

## Synthesis of $\text{TiO}_2/\text{SiO}_2\text{-B}_2\text{O}_3$ Ternary Nanocomposites: Influence of Interfacial Properties on their Photocatalytic Activities with High Resolution Mass Spectrometry Monitoring

Susana F. Resende, Rafael L. Gouveia, Bernardo S. Oliveira, Wander L. Vasconcelos and Rodinei Augusti\*

Universidade Federal de Minas Gerais, Av. Antônio Carlos, 6627, Pampulha, 31270-901 Belo Horizonte-MG, Brazil

An investigation on unusual interface properties of unprecedented ternary composites, formed by the inclusion of assorted proportions of  $\text{B}_2\text{O}_3$  into  $\text{TiO}_2/\text{SiO}_2$  structure, is conducted herein. The influences of  $\text{B}_2\text{O}_3$  content and calcination temperature were evaluated. The precursor  $\text{TiO}_2/\text{SiO}_2$  material was synthesized via a simple sol-gel procedure that was followed by  $\text{B}_2\text{O}_3$  inclusion via maceration and calcination. The materials were fully characterized and their photocatalytic performance to degrade the Indigo Carmine dye investigated. The material prepared with a B/Ti molar ratio of 1 and at calcination temperature of 350 °C ( $\text{B}_{1-350}$ ) showed the best performance, with a superior photocatalytic activity than that of commercial  $\text{TiO}_2$ . The presence of  $\text{B}_2\text{O}_3\text{-TiO}_2\text{-SiO}_2$  interfaces in the structure of such material was of critical importance in producing a material with these attractive features. Finally, high resolution mass spectrometry monitoring allowed for the characterization of the main degradation products formed under these conditions.

**Keywords:**  $\text{B}_2\text{O}_3\text{-TiO}_2\text{-SiO}_2$  ternary nanocomposites, structural defects, photocatalytic activity, degradation of Indigo Carmine, by-products characterization, high resolution mass spectrometry

### Introduction

In recent years, several investigations<sup>1,2</sup> have been dedicated to the improvement of the photocatalytic performance of  $\text{TiO}_2$ . This is due to its appealing properties, such as strong oxidizing ability for the decomposition of organic pollutants, remarkable chemical stability and low cost/toxicity.<sup>3</sup> However, some drawbacks, such as its relatively large energy band gap (3.2 and 3.0 eV for anatase and rutile, respectively) and its low quantum yield, prevent its further application in photocatalytic processes.<sup>4</sup> Hence, a variety of strategies has been developed in an attempt to produce modified materials with a superior photocatalytic proficiency.<sup>5</sup>

In this context, the incorporation of other oxides, such as  $\text{SiO}_2$ ,  $\text{ZrO}_2$ ,  $\text{WO}_3$  and  $\text{Al}_2\text{O}_3$ , into the  $\text{TiO}_2$  structure has been widely studied.<sup>6-10</sup> It is well-known that the addition of  $\text{SiO}_2$  to  $\text{TiO}_2$  improves the specific surface area (SSA) of the modified material, thus, increasing the adsorption rate of organic pollutants.<sup>11</sup> In our previous work,<sup>12</sup> it was shown that the presence of  $\text{SiO}_2$  inhibits the growth

of the anatase crystals during  $\text{TiO}_2$  calcination, retarding the transformation of anatase to rutile phase. Guan *et al.*<sup>13</sup> suggested that the addition of  $\text{SiO}_2$  can increase the concentration of hydroxyl groups on the  $\text{TiO}_2$  surface, resulting in samples with improved photocatalytic and hydrophilic properties. All of these factors can lead to an increase in the number of active sites, as well as a better efficiency for the separation of photogenerated charges, thus enhancing the photocatalytic activity, as proven by several studies.<sup>14,15</sup>

$\text{B}_2\text{O}_3$  is another oxide that has been incorporated into the  $\text{TiO}_2$  structure to produce a material with superior performance. This possibility has been reported, however, in just few studies.<sup>16-18</sup> To the best of our knowledge, a detailed study regarding the role of the  $\text{B}_2\text{O}_3\text{-TiO}_2$  interfaces on the superior photocatalytic activity of this type of material is unprecedented.

Taking into account these remarks, the synthesis of  $\text{TiO}_2/\text{SiO}_2\text{-B}_2\text{O}_3$  ternary nanocomposites is reported herein. For this purpose, we evaluated the influence of two key variables during the nanocomposite preparation: the boron content and the calcination temperature. These materials were synthesized by sol-gel route followed by

\*e-mail: augusti.rodinei@gmail.com

hydrothermal and calcination treatments, and characterized by nitrogen sorption tests, X-ray diffraction (XRD), diffuse reflectance spectroscopy (DRS), Fourier transform infrared spectroscopy (FTIR) and scanning electron microscopy (SEM). The performance of all synthesized TiO<sub>2</sub>/SiO<sub>2</sub>-B<sub>2</sub>O<sub>3</sub> nanocomposites towards the photodegradation of a prototype pollutant (Indigo Carmine dye) in an aqueous solution and under irradiation, provided by a commercial fluorescent lamp, was measured by UV-Vis spectrometry. Chemical structures of the by-products formed under these conditions were proposed based on the data obtained via a direct monitoring by electrospray ionization high-resolution mass spectrometry (ESI-HRMS). The mineralization rate was also estimated by measuring the oxygen consumption. Indigo Carmine was chosen as a prototype substrate because it is a synthetic dye widely used as a coloring agent or additive in industry. Moreover, it is quite harmful to aquatic life and often used as a model pollutant in photocatalytic studies due to its advantageous characteristics, such as ease of access, low cost and easy degradation monitoring by UV-Vis spectrophotometry. The photocatalytic activity of the best material was then compared with those provided by two types of commercially available TiO<sub>2</sub>: TiO<sub>2</sub> (99% anatase) and TiO<sub>2</sub> P25 (80% anatase, 20% rutile).

## Experimental

### Synthesis

The Pluronic® F127 triblock copolymer [(EO)<sub>106</sub>(PO)<sub>70</sub>(EO)<sub>106</sub>, M: 12600] was used as a structural directing agent. Titanium(IV) isopropoxide (TIP), tetraethoxysilane (TEOS) and boric acid (H<sub>3</sub>BO<sub>3</sub>) were used as precursors for TiO<sub>2</sub>, SiO<sub>2</sub> and boron, respectively. Sulfuric acid (H<sub>2</sub>SO<sub>4</sub>) and 2,4-pentanedione (acac) were employed as acidifying and complexing agents, respectively. All reagents were purchased from Sigma-Aldrich and used as received without additional treatment. To conduct the comparative photocatalytic tests, the following commercial materials were evaluated: TiO<sub>2</sub> (99% anatase) from Sigma-Aldrich, and TiO<sub>2</sub> P25 (80% anatase, 20% rutile) from Evonik.

Initially, 1.64 g of the F127 copolymer was dissolved in 100 mL of deionized water (at 40 °C) containing H<sub>2</sub>SO<sub>4</sub> sufficient to maintain the pH value at approximately 0.65. After complete the copolymer dissolution, 4.1 mmol of TEOS were added to this solution, which was kept under constant stirring. To this solution, it was added a mixture of TIP (41.4 mmol) and acac (41.4 mmol) under vigorous stirring. The final solution was then maintained at 55 °C for 2 h without stirring. After several minutes, a light

yellow colloidal suspension was formed. The hydrothermal treatment was conducted by leaving the as-prepared suspension at 110 °C for 6 h. The resulting solid (consisting of TiO<sub>2</sub>/SiO<sub>2</sub> nanocomposite particles) was filtered and washed with water and then dried overnight in an oven at 60 °C.

To obtain the TiO<sub>2</sub>/SiO<sub>2</sub>-B<sub>2</sub>O<sub>3</sub> nanocomposites, the TiO<sub>2</sub>/SiO<sub>2</sub> particles were ground with different amounts of H<sub>3</sub>BO<sub>3</sub> and calcined at different temperatures (350, 450 or 550 °C). The nomenclature for the synthesized materials was B<sub>x-y</sub>, where x is the molar ratio B/Ti (R<sub>B</sub>) and y is the calcination temperature. Therefore, the calcined samples at 450 °C, B<sub>0-450</sub>, B<sub>0.125-450</sub>, B<sub>0.25-450</sub>, B<sub>0.5-450</sub>, B<sub>1-450</sub>, B<sub>2-450</sub> and B<sub>4-450</sub>, were prepared using R<sub>B</sub> of 0, 0.125, 0.25, 0.5, 1, 2 and 4, respectively. On the other hand, the B<sub>1-350</sub>, B<sub>1-450</sub> and B<sub>1-550</sub> samples were prepared using R<sub>B</sub> = 1 and calcination temperatures of 350, 450 and 550 °C, respectively. Commercial TiO<sub>2</sub> were named anatase (TiO<sub>2</sub> Sigma-Aldrich) and P25 (TiO<sub>2</sub> Evonik). The SiO<sub>2</sub>/TiO<sub>2</sub> molar ratio was kept constant at 0.1 for each nanocomposite, whereas the B/Ti molar ratio (R<sub>B</sub>) was varied from 0 to 4.

### Characterizations

Nitrogen sorption tests were performed in an Autosorb-1C apparatus. Samples used in these analyses were previously degassed at 130 °C for up to 48 h under vacuum. SSA and pore size distribution were assessed by the multipoint BET (Brunauer, Emmett and Teller) and NLDFT (non-local density functional theory) methods, respectively. XRD analysis was carried out in a Philips-PANalytical PW17-10 diffractometer using Cu K $\alpha$  radiation and operating at 40 kV and 40 mA. XRD patterns were collected in the 2 $\theta$  range of 10 to 90°, using a scan velocity of 0.06 degree min<sup>-1</sup>. The identification of the crystalline phases was performed using the JCPDS (International Centre for Diffraction Data®) file numbers 21-1272 and 30-0199 for anatase and sassolite (H<sub>3</sub>BO<sub>3</sub>), respectively. The TiO<sub>2</sub> crystallite size was assessed using the Scherrer equation and considering XRD peaks at 25.3° for anatase. Diffuse reflectance spectra were obtained in a UV-Vis-NIR instrument (Hitachi model U-3501) with the diffuse reflectance accessory equipped with an integrating sphere. BaSO<sub>4</sub> was used as reference material and for sample dilutions. The gap values were calculated using the Kubelka-Munk function. Samples for the FTIR spectra were prepared as pellets with KBr and examined in a FTIR/FIR spectrometer (PerkinElmer model Frontier). The spectra were recorded from 4000 to 350 cm<sup>-1</sup>, with resolution of 4 cm<sup>-1</sup> and acquisition of 128 scans. SEM images were obtained on a FEI QUANTA 3D field emission

gun scanning electron microscope (FEG-SEM). Samples were sputtercoated with a carbon layer of about 5 nm thickness before the SEM analysis.

### Photocatalytic tests

The photocatalytic activities of the  $\text{TiO}_2/\text{SiO}_2\text{-B}_2\text{O}_3$  nanocomposites were estimated by measuring the rate of degradation of the Indigo Carmine dye in aqueous suspension. The degradation tests were preceded by adsorption tests in the absence of light. Photolysis, hydrolysis and tests with pure  $\text{B}_2\text{O}_3$  were also performed as controls. All photocatalytic tests were performed in triplicate in order to evaluate reproducibility. The reactor used for the photocatalytic tests consisted of a wooden box coated with aluminum foil. The dimensions of the reactor were 55 cm height, 85 cm length and 30 cm depth (Figure S1, in the Supplementary Information (SI) section, shows the design of the reactor). In a typical run, 30 mg of the ternary nanocomposite were added to 250 mL of Indigo Carmine solution ( $10 \text{ mg L}^{-1}$ ). This suspension was kept under constant magnetic stirring and submitted to irradiation by a commercial fluorescent lamp (power of 32 W, Taschibra model TKS 32-1 NJY). The emission spectrum of this lamp is provided in Figure S2 (in the SI section). Aliquots of 5 mL were collected at the following times: 0, 5, 15, 30, 45, 60, 90 and 120 min. The aliquots were centrifuged at 4000 rpm for 10 min in a model Centrifio 80-2B centrifuge. The supernatant was collected and filtered through a disposable filter unit for syringes (Millex<sup>®</sup>, PVDF,  $\varnothing = 0.45 \mu\text{m}$ ). The Indigo Carmine concentration in each aliquot was estimated using a UV-Vis spectrophotometer (Varian, model Cary 50 Conc) working at 610 nm ( $\lambda_{\text{max}}$  for Indigo Carmine). Full scan UV-Vis spectra (from 300 to 700 nm) were also recorded for some samples. The apparent reaction rate constant ( $k_{\text{app}}$ ) for each material was calculated during the first 60 min of reaction and by considering a pseudo-first order model. The pH value of the solution, monitored by a pHmeter (HANNA model HI98128), remained roughly constant (approximately 4.5) during the experiment. Chemical structures of the by-products were proposed based on the data obtained via direct infusion ESI-HRMS analyzes. The analyses were performed on a hybrid mass spectrometry system. The mass spectrometer (IT-TOF, Shimadzu Corporation, Kyoto, Japan) provides high sensitivity and accuracy with a resolving power over 10,000. The mass spectrometer was equipped with an electrospray ionization (ESI) source operating in the negative ( $-3.5 \text{ kV}$ ) mode and with a nebulizer gas ( $\text{N}_2$ ) at a flow rate of  $1.5 \text{ L min}^{-1}$ . The interface and CDL (curved desolvation line) were operated

at constant temperature of  $200 \text{ }^\circ\text{C}$ . A mass-to-charge ( $m/z$ ) range of 100-500 was recorded for each aliquot. The samples ( $10 \mu\text{L}$ ) were directly infused into the ESI source via an autosampler. Mineralization rates were estimated according to the oxygen consumption method that makes use of potassium permanganate to oxidize the organic material in solution. A detailed description about this procedure is provided in the directive NBR 10739/1989.<sup>19</sup> Chemical oxygen demand (COD) and total organic carbon (TOC) methods could not be applied herein due to the low concentrations of Indigo Carmine employed.

## Results and Discussion

### B/Ti molar ratio ( $R_B$ )

Figure 1 shows the XRD patterns obtained for the produced materials, i.e.,  $B_{0-450}$ ,  $B_{0.125-450}$ ,  $B_{0.25-450}$ ,  $B_{0.5-450}$ ,  $B_{1-450}$ ,  $B_{2-450}$  and  $B_{4-450}$ . As noted, all samples showed anatase as the crystal phase, whereas no peaks associated with the brookite or rutile phases were found. The peaks at  $14.58$  and  $27.94^\circ$  ( $2\theta$ ) confirm the formation of the boron trioxide ( $\text{B}_2\text{O}_3$ ) crystalline phase.

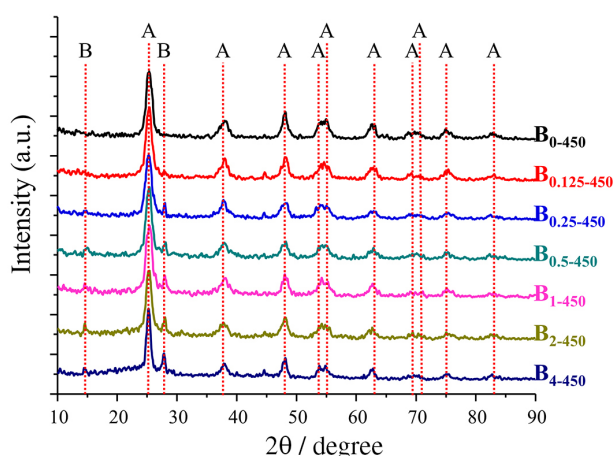
Table 1 shows the physicochemical properties of the synthesized and commercial materials. Compared with  $B_{0-450}$ , the  $\text{TiO}_2/\text{SiO}_2\text{-B}_2\text{O}_3$  nanocomposites ( $B_{0.125-450}$ ,  $B_{0.25-450}$ ,  $B_{0.5-450}$ ,  $B_{1-450}$ ,  $B_{2-450}$  and  $B_{4-450}$ ) display no significant changes in the crystallite size, confirming the results presented in Figure 1. The presence of  $\text{SiO}_2$  and the formation of  $\text{B}_2\text{O}_3$  phase may obstruct the nucleation of anatase nanoparticles, allowing only a slight increase in the average crystallite size. As seen in Table 1, the gap value oscillated between 3.32 and 3.29 eV for the  $B_{0-450}$  to  $B_{4-450}$  materials. This finding indicates that the  $\text{B}_2\text{O}_3$  incorporation has no significant influence on this parameter. The data displayed in Table 1 for the  $B_{0-450}$  to  $B_{4-450}$  materials also indicate that an increase in  $R_B$  causes a decrease in SSA and in the average pore size. That is probably because the  $\text{B}_2\text{O}_3$  phase deposited on the nanocomposite surface blocks the pores of the material leading to the reduction in the values of both parameters.

Figure 2 shows the FTIR analysis of the  $B_{0-450}$ ,  $B_{0.125-450}$ ,  $B_{0.25-450}$ ,  $B_{1-450}$  and  $B_{4-450}$  materials. The bands at  $3400$  and  $1630 \text{ cm}^{-1}$  are attributed to vibrations of surface water and O–H stretching.<sup>20</sup> The band at approximately  $3220 \text{ cm}^{-1}$  can be attributed to B–O bond vibrations.<sup>20</sup> In fact, the intensity of this band increases by increasing  $R_B$ . The bands between  $2260$  and  $2510 \text{ cm}^{-1}$  are related to B–H vibrations.<sup>21</sup> The bands at  $1440$  and  $1200 \text{ cm}^{-1}$  are associated with the B–O bond in boroxol rings.<sup>20,22,23</sup> At  $1125$  and  $1050 \text{ cm}^{-1}$ , a Si–O–Si vibration can be observed.<sup>16,24</sup> In this region ( $1000$  to

**Table 1.** Physicochemical properties of the synthesized (B<sub>0-450</sub>, B<sub>0.125-450</sub>, B<sub>0.25-450</sub>, B<sub>0.5-450</sub>, B<sub>1-450</sub>, B<sub>2-450</sub>, B<sub>4-450</sub>, B<sub>1-350</sub> and B<sub>1-550</sub>) and commercial materials (TiO<sub>2</sub>-anatase and TiO<sub>2</sub>-P25)

Sample	SSA / (m <sup>2</sup> g <sup>-1</sup> )	Pore size / nm	Pore volume / (cm <sup>3</sup> g <sup>-1</sup> )	Crystallite size / nm	Gap / eV	k <sub>app</sub> / min <sup>-1</sup>	R <sup>2</sup>
B <sub>0-450</sub>	159.00	5.90	0.2065	14.46	3.32	0.0027	0.9934
B <sub>0.125-450</sub>	115.90	5.90	0.1736	14.46	3.31	0.0059	0.9998
B <sub>0.25-450</sub>	105.70	5.30	0.1642	14.14	3.30	0.0088	0.9859
B <sub>0.5-450</sub>	56.97	5.30	0.0984	14.26	3.32	0.0107	0.9900
B <sub>1-450</sub>	9.33	5.30	0.0182	14.60	3.31	0.0164	0.9901
B <sub>2-450</sub>	0.67	4.18	0.0020	14.66	3.31	0.0093	0.9898
B <sub>4-450</sub>	0.86	1.69	0.0012	17.88	3.29	0.0030	0.9863
B <sub>1-350</sub>	7.66	5.90	0.0105	12.05	3.30	0.0227	0.9916
B <sub>1-550</sub>	6.64	6.81	0.0158	24.09	3.29	0.0042	0.9935
Hydrolysis	–	–	–	–	–	0.0000008	0.9949
Photolysis	–	–	–	–	–	0.0003	0.9866
B <sub>2</sub> O <sub>3</sub>	–	–	–	–	–	0.00009	0.9898
TiO <sub>2</sub> -anatase	11 <sup>a</sup>	–	–	68.08 <sup>a</sup>	3.29	0.0049	0.9975
TiO <sub>2</sub> -P25	50 ± 15 <sup>a</sup>	–	–	21 <sup>a</sup>	3.29	0.0113	0.9929

<sup>a</sup>Data provided by the manufacturer. Gap: energy band gap; R<sup>2</sup>: determination coefficient.



**Figure 1.** XRD patterns for the B<sub>0-450</sub> to B<sub>4-450</sub> materials. The letters 'A' and 'B' indicate peaks attributed to the anatase crystalline phase and sassolite (B<sub>2</sub>O<sub>3</sub>), respectively.

1200 cm<sup>-1</sup>), C–O vibrational modes may also appear due to organic waste from the syntheses. The broad band between 900 and 400 cm<sup>-1</sup> is associated with the vibrational modes of Ti–O in TiO<sub>2</sub>.<sup>23,24</sup> Finally, the increasing of R<sub>B</sub> causes the appearance of bands at 810 and 540 cm<sup>-1</sup> (B–O deformation) and 644 cm<sup>-1</sup> (stretching B–B).<sup>25</sup> Note that the appearance of these bands decreases the intensity of the TiO<sub>2</sub> band, corroborating to the proposal of a thick B<sub>2</sub>O<sub>3</sub> layer deposited on the TiO<sub>2</sub>/SiO<sub>2</sub> nanocomposites particles. SEM micrographs of B<sub>0-450</sub>, B<sub>1-450</sub> and B<sub>4-450</sub> are displayed in Figure S3 (in the SI section). In these images, changes in the morphology of the particles are clearly observed.

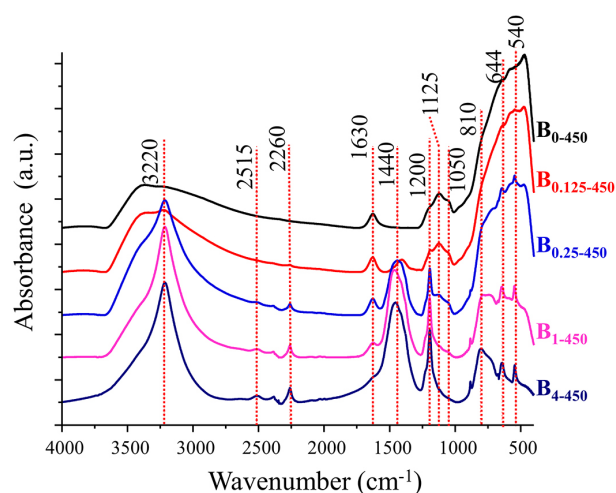


**Figure 2.** FTIR spectra for the B<sub>0-450</sub>, B<sub>0.125-450</sub>, B<sub>0.25-450</sub>, B<sub>1-450</sub> and B<sub>4-450</sub> materials.

Figure 3 shows the results of the tests dealing with the photocatalytic activities of the TiO<sub>2</sub>/SiO<sub>2</sub>-B<sub>2</sub>O<sub>3</sub> materials. The k<sub>app</sub> and R<sup>2</sup> (determination coefficient) values of each material are shown in Table 1. The adsorption-desorption equilibrium was reached after 30 min. The activity increases with R<sub>B</sub> until it reaches a maximum in R<sub>B</sub> = 1 (B<sub>1-450</sub>). Taking into account that this sample does not have the highest SSA (Table 1), these results therefore seem to indicate that the presence of an interfacial B<sub>2</sub>O<sub>3</sub> phase is essential to produce materials with enhanced photocatalytic activities. For the material B<sub>1-450</sub>, the B<sub>2</sub>O<sub>3</sub> layer, which is deposited on the surface of the nanoparticles and is part of

an interface with the other two oxides, helps to improve the degradation rate due to the formation of traps for the photogenerated charges.<sup>4</sup> However, for the materials with  $R_B > 1$  ( $B_{2-450}$  and  $B_{4-450}$ ), these traps drastically increase and act as centers of charge recombination, which disfavors the photocatalytic process.<sup>22</sup> Furthermore, for these materials ( $B_{2-450}$  and  $B_{4-450}$ ), the thicker  $B_2O_3$  layer probably hampers the radiation to reach the  $TiO_2$  surface.<sup>16</sup> The difference in activity of these materials, as well as the results obtained by mass spectrometry (discussed following in this paper), confirms that the dye did not act as a sensitizer agent for the photocatalysts. The  $B_{1-450}$  sample was therefore chosen as the prototype material to be further evaluated, as following described in this article.

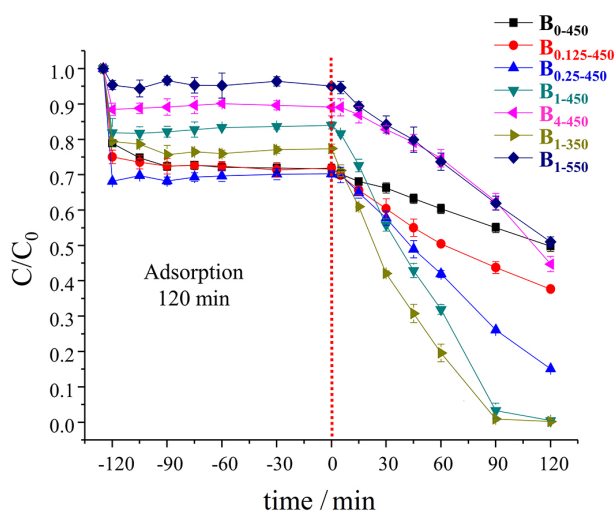


**Figure 3.** Photocatalytic activities of the degradation of the Indigo Carmine dye in aqueous solution for the  $TiO_2/SiO_2-B_2O_3$  materials.

#### Effect of calcination temperature

Figure 4 shows the XRD patterns recorded for the  $B_{1-350}$ ,  $B_{1-450}$  and  $B_{1-550}$  samples. As the calcination temperature increases, narrow peaks emerge indicating a higher crystallinity, which can be confirmed by the increase in the average crystallite size (Table 1). Moreover, the rutile phase is not detected, even at 550 °C, corroborating the previous assumption that  $SiO_2$  and  $B_2O_3$  can suppress diffusion between the anatase particles, thus, limiting anatase to rutile transformation. It was verified that the calcination temperature has no evident effect in the gap value. However, the  $B_{1-350}$  and  $B_{1-550}$  samples showed higher average pore size and lower SSA than  $B_{1-450}$ . Hence, the calcination at 350 °C is probably not sufficient to remove the organic residues that can block the smaller pores and yields a material with a higher average pore size and a smaller SSA. At higher temperatures (550 °C), however, the formation of larger nanoparticles results in the closing of the smaller pores,

thus, leading to an increase of the average pore size and a reduction of SSA. The FTIR analysis of the  $B_{1-350}$ ,  $B_{1-450}$  and  $B_{1-550}$  samples (not shown) presents the same profile as that shown in Figure 2 for  $B_{1-450}$ . The only exception was the reduction in the intensities of the bands at approximately 3400 and 1630  $cm^{-1}$  from  $B_{1-350}$  to  $B_{1-550}$  that indicates the loss of water at higher temperatures.<sup>20</sup>

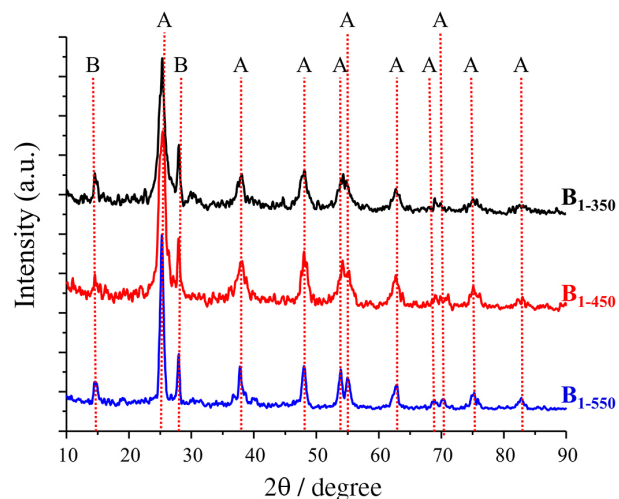


**Figure 4.** XRD patterns for the  $B_{1-350}$ ,  $B_{1-450}$  and  $B_{1-550}$  materials. The letters 'A' and 'B' indicate peaks attributed to the anatase crystalline phase and sassolite ( $B_2O_3$ ), respectively.

The results for the photocatalytic activities of  $B_{1-350}$ ,  $B_{1-450}$  and  $B_{1-550}$  samples is displayed in Table 1 ( $k_{app}$  and  $R^2$ ) and Figure 3. These data indicate that higher calcination temperatures cause a decrease in the degradation rate. After 90 min, the  $B_{1-350}$  and  $B_{1-450}$  samples showed degradation rates of almost 100%, while the  $B_{1-550}$  sample showed approximately 40% degradation. Higher temperatures improve the average crystallite size, which increases not only the distance that photogenerated charges must overcome to reach the surface but also the charge recombination rate.<sup>26</sup> The reduction of SSA at higher temperatures also minimizes the availability of active sites. Furthermore, full scan absorption spectra (not shown) of the reaction aliquots (from 300 to 700 nm) indicate no formation of by-products that absorb in the visible region. Therefore, the absorbance at 610 nm (the  $\lambda_{max}$  of Indigo Carmine) was a reliable measurement to determine the concentration of the remaining dye in solution.

Analyzes by direct infusion electrospray ionization high resolution mass spectrometry (ESI-HRMS) was conducted aiming at detecting at least the most abundant by-products, probably formed under these conditions. ESI-HRMS is a key technique for the identification of by-products resulting from the degradation of water

contaminants, and therefore has played an important role in elucidating degradation pathways.<sup>27</sup> Figure 5 shows the mass spectra (negative mode) of aliquots collected at times 0 and 120 min for the three photocatalytic systems (B<sub>1-350</sub>, B<sub>1-450</sub> and B<sub>1-550</sub>). Note that the mass spectra for such photocatalytic systems showed the same profile, the only difference being the relative intensity of each ion. In the mass spectrum of the initial aliquots, the following ions that refer to Indigo Carmine are clearly noticed (Table 2 and Figure 5):  $m/z$  209.9863 (doubly-deprotonated Indigo Carmine: [C<sub>16</sub>H<sub>8</sub>N<sub>2</sub>O<sub>8</sub>S<sub>2</sub>]<sup>2-</sup> or [IC]<sup>2-</sup>), and  $m/z$  442.9626 (mono-deprotonated Indigo Carmine: [C<sub>16</sub>H<sub>9</sub>N<sub>2</sub>O<sub>8</sub>S<sub>2</sub>]<sup>-</sup> or [IC + H]<sup>-</sup>).

Non-covalent species derived directly from Indigo Carmine are also detectable in this mass spectrum (Table 2 and Figure 5): [(IC)<sub>2</sub> + H]<sup>3-</sup> of  $m/z$  287.6452 and [(IC)<sub>3</sub> + 2H]<sup>4-</sup> of  $m/z$  326.4745. After 120 min of exposure to the photocatalytic systems, these anions are no longer detected only in the mass spectrum of the aliquot collected

from the B<sub>1-350</sub> system. These results confirm therefore that the B<sub>1-350</sub> photocatalyst possesses indeed a superior efficiency to degrade Indigo Carmine in comparison to the other systems (B<sub>1-450</sub> and B<sub>1-550</sub>). The emergence of extra anions (not detectable in the original solutions) in the mass spectra of the aliquots collected after an exposure time of 120 min is attributed to the formation of by-products (Figure 5). Table 2 displays a list of these anions and their respective molecular formula. The errors between the theoretical and experimental  $m/z$  values were smaller than 11.24 ppm and then support the proposed molecular formula. All these by-products originate from an initial oxidation of the Indigo Carmine molecule followed by successive oxidation/ring hydroxylations. Note, as expected, that the mass spectrum of the B<sub>1-350</sub> aliquot exhibit these by-products at higher intensities than in the mass spectra of the other systems. Finally, based on these experimental data as well as on previous studies reported in the literature, a route for the degradation of Indigo Carmine



**Figure 5.** High resolution mass spectrometry (HRMS) recorded for aliquots collected after 0 and 120 min of exposure to the photocatalytic systems: B<sub>1-350</sub>, B<sub>1-450</sub> and B<sub>1-550</sub>. The molecular formulae attributed to some by-products are indicated in Table 2.

**Table 2.** High-resolution mass spectrometry data and molecular formula inferred for the by-products generated during the photodegradation of Indigo Carmine dye in water by the three photocatalytic systems: B<sub>1-350</sub>, B<sub>1-450</sub> and B<sub>1-550</sub>

Anion	Molecular formulae	<i>m/z</i> (theoretical)	<i>m/z</i> (experimental)	Error / ppm	DBE
Anions derived from Indigo Carmine dye (IC)					
[IC] <sup>2-</sup>	C <sub>16</sub> H <sub>8</sub> N <sub>2</sub> O <sub>8</sub> S <sub>2</sub>	209.9867	209.9863	-1.90	13.0
[IC + H] <sup>-</sup>	C <sub>16</sub> H <sub>9</sub> N <sub>2</sub> O <sub>8</sub> S <sub>2</sub>	442.9625	442.9626	0.23	13.0
[(IC) <sub>2</sub> + H] <sup>3-</sup>	C <sub>32</sub> H <sub>17</sub> N <sub>4</sub> O <sub>16</sub> S <sub>4</sub>	287.6453	287.6452	-0.35	25.0
[(IC) <sub>3</sub> + 2H] <sup>4+</sup>	C <sub>48</sub> H <sub>26</sub> N <sub>6</sub> O <sub>24</sub> S <sub>6</sub>	326.4746	326.4745	-0.31	37.0
By-products (anionic form)					
[1] <sup>-</sup>	C <sub>8</sub> H <sub>5</sub> NO <sub>5</sub> S	225.9816	225.9810	-2.66	7.0
[2] <sup>-</sup>	C <sub>8</sub> H <sub>5</sub> NO <sub>6</sub> S	241.9765	241.9773	3.31	7.0
[3] <sup>-</sup>	C <sub>7</sub> H <sub>6</sub> NO <sub>5</sub> S	215.9972	215.9979	3.24	5.0
[4] <sup>-</sup>	C <sub>8</sub> H <sub>4</sub> NO <sub>7</sub> S	257.9714	257.9743	11.24	7.0
[5] <sup>-</sup>	C <sub>6</sub> H <sub>3</sub> O <sub>6</sub> S	202.9656	202.9651	-2.46	5.0

DBE: double-bond equivalence.

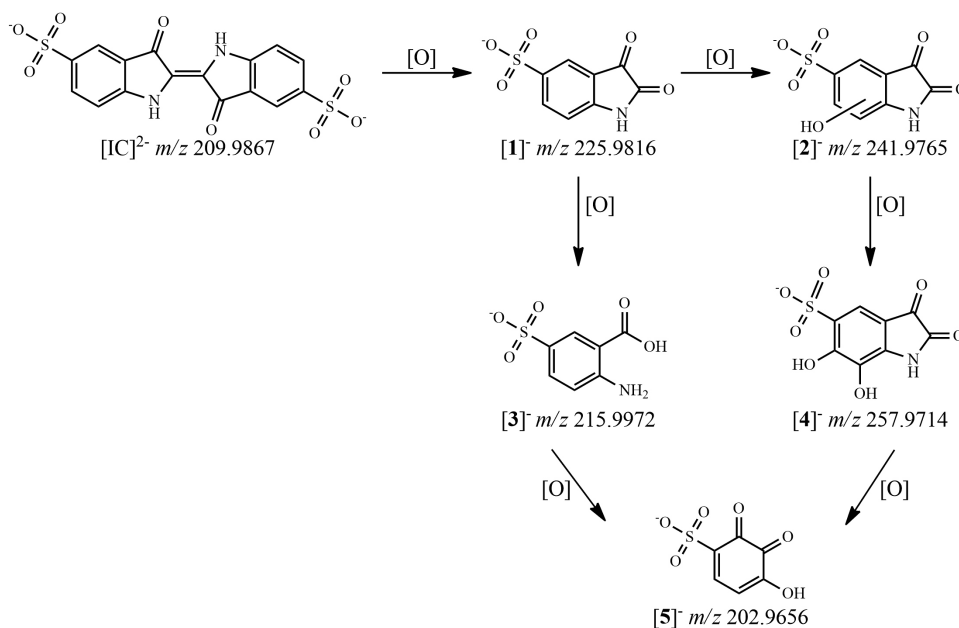
in aqueous medium by the three photocatalytic systems could therefore be proposed, as displayed in Figure 6.<sup>27,28</sup> Due to its superior photocatalytic efficiency, the B<sub>1-350</sub> sample was selected to accomplish comparative tests with commercial TiO<sub>2</sub>.

#### Photocatalytic efficiency: comparative tests

To conduct the comparative tests, the commercial materials (anatase and P25) were evaluated. Table 1 and Figure 7 summarize the results of the photocatalytic activities of these materials as well as B<sub>0-450</sub>, B<sub>1-350</sub> and controls tests. Note that the control experiments did not

produce any significant degradation of the Indigo Carmine dye. The B<sub>1-350</sub> material proved to be more effective than both commercial samples, with a *k*<sub>app</sub> that is twice that of P25. The B<sub>1-350</sub> sample has a lower SSA than the other materials, proving that the B<sub>2</sub>O<sub>3</sub>-TiO<sub>2</sub>-SiO<sub>2</sub> interfaces (by reasons previously stated) probably explains this superior photocatalytic activity.

Finally, data on oxygen consumption indicated that only the B<sub>0.5-450</sub>, B<sub>1-450</sub>, B<sub>2-450</sub>, B<sub>1-350</sub>, anatase and P25 systems were able to cause mineralization, but at low rates. Moreover, the systems comprised by P25 (the most widely used photocatalyst) and B<sub>1-350</sub> yielded the best results, i.e., rates of about 11.5%.

**Figure 6.** Proposed route for the photodegradation of Indigo Carmine dye in water as induced by the three photocatalysts: B<sub>1-350</sub>, B<sub>1-450</sub> and B<sub>1-550</sub>.

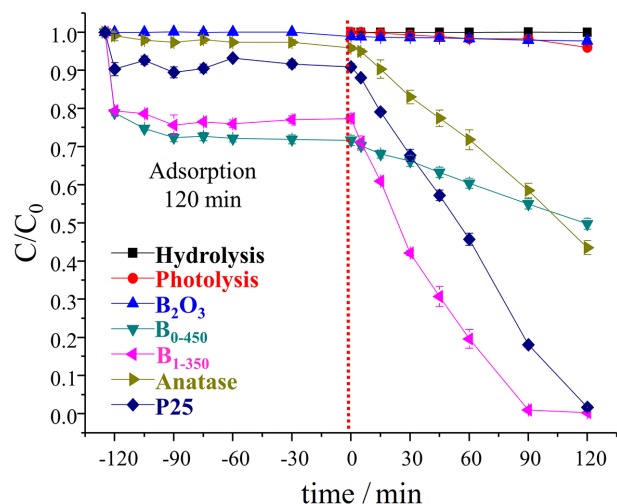


**Figure 7.** Photocatalytic activities of the degradation of the Indigo Carmine dye in aqueous solution for hydrolysis, photolysis, B<sub>2</sub>O<sub>3</sub>, B<sub>0-450</sub>, B<sub>1-350</sub> and commercial TiO<sub>2</sub> materials.

## Conclusions

TiO<sub>2</sub>/SiO<sub>2</sub> nanocomposites were obtained in a single step and at low temperature using a synthetic procedure that employs water as the solvent. B<sub>2</sub>O<sub>3</sub> inclusion allowed the attainment of materials with improved photocatalytic activities, as verified in degradation tests with a common organic pollutant (the Indigo Carmine dye). SiO<sub>2</sub> and B<sub>2</sub>O<sub>3</sub> contributed to stabilize the anatase phase, even when a calcination at 550 °C was applied. The optimized material was obtained with a B/Ti ratio (R<sub>B</sub>) of 1 and by employing a calcination temperature of 350 °C. This material showed a performance superior to those of commercial TiO<sub>2</sub> materials in causing the depletion of Indigo Carmine. Although the surface area is of fundamental importance for photocatalytic processes, this work demonstrated that the interactions that occur at the material interfaces are also critical. Hence, the B<sub>2</sub>O<sub>3</sub>-TiO<sub>2</sub>-SiO<sub>2</sub> interfaces seem to act as sites of charge separation up to a maximum content of B<sub>2</sub>O<sub>3</sub>. After this maximum, the B<sub>2</sub>O<sub>3</sub> layer causes the opposite effect. The reactions were monitored by direct infusion electrospray ionization high resolution mass spectrometry which revealed that Indigo Carmine is efficiently degraded and that the main by-products are continuously formed by successive oxidations/hydroxylations. It is noteworthy that in all of the degradation experiments a common fluorescent lamp was used as the light source. Fluorescent lamps are easily accessible, of low cost and consume less power than the lamps commonly used in similar photocatalytic experiments. These results therefore reveal that this TiO<sub>2</sub>/SiO<sub>2</sub>-B<sub>2</sub>O<sub>3</sub> nanocomposite can be used without the need of high energy light sources and has clear potential to be employed for the treatment of real effluents contaminated with organic matter.

## Supplementary Information

Supplementary data are available free of charge at <http://jbcs.sbq.org.br> as PDF file.

## Acknowledgments

The authors thank the financial support from CAPES and CNPq/FAPEMIG (agreement recorded in SICONV: 793988/2013). We kindly acknowledge the Microscopy Center at the Universidade Federal de Minas Gerais for the execution of the SEM tests and Prof Vicente Buono for the attainment of the XRD data. R. L. G. and B. S. O. are also grateful to the sponsorship from the Pró-Reitoria de Pesquisa of Universidade Federal de Minas Gerais.

## References

- Fujishima, A.; Zhang, X.; Tryk, D.; *Surf. Sci. Rep.* **2008**, *63*, 515.
- Henderson, M. A.; *Surf. Sci. Rep.* **2011**, *66*, 185.
- Nakata, K.; Fujishima, A.; *J. Photochem. Photobiol., C* **2012**, *13*, 169.
- Dozzi, M. V.; Selli, E.; *J. Photochem. Photobiol., C* **2013**, *14*, 13.
- Kumar, S. G.; Devi, L. G.; *J. Phys. Chem. A* **2011**, *115*, 1321.
- Kim, J.; Song, K. C.; Foncillas, S.; Pratsinis, S. E.; *J. Eur. Ceram. Soc.* **2001**, *21*, 2863.
- Calleja, G.; Serrano, D. P.; Sanz, R.; Pizarro, P.; *Microporous Mesoporous Mater.* **2008**, *111*, 429.
- Bai, S.; Liu, H.; Sun, J.; Tian, Y.; Chen, S.; Song, J.; Luo, R.; Li, D.; Chen, A.; Liu, C.-C.; *Appl. Surf. Sci.* **2015**, *338*, 61.
- Ide, Y.; Koike, Y.; Ogawa, M.; *J. Colloid Interface Sci.* **2011**, *358*, 245.
- He, C.; Tian, B.; Zhang, J.; *J. Colloid Interface Sci.* **2010**, *344*, 382.
- Gao, X.; Wachs, I. E.; *Catal. Today* **1999**, *51*, 233.
- Resende, S. F.; Nunes, E. H. M.; Houmard, M.; Vasconcelos, W. L.; *J. Colloid Interface Sci.* **2014**, *433*, 211.
- Guan, K.; Lu, B.; Yin, Y.; *Surf. Coat. Technol.* **2003**, *173*, 219.
- Anderson, C.; Bard, A. J.; *J. Phys. Chem.* **1995**, *99*, 9882.
- Vohra, M. S.; Lee, J.; Choi, W.; *J. Appl. Electrochem.* **2005**, *35*, 757.
- Jung, K. Y.; Park, S. B.; Ihm, S.-K.; *Appl. Catal., B* **2004**, *51*, 239.
- Moon, S. C.; Mametsuka, H.; Suzuki, E.; Nakahara, Y.; *Catal. Today* **1998**, *45*, 79.
- Zhu, L. Y.; Wang, X. Q.; Zhang, G. H.; Ren, Q.; Xu, D.; *Appl. Catal., B* **2011**, *103*, 428.
- ABNT, Associação Brasileira de Normas Técnicas, 1989. Available at <http://www.abntcatalogo.com.br/norma.aspx?ID=4635>, accessed in June 2016.

20. Wang, Y.; Xue, X.; Yang, H.; *Ceram. Int.* **2014**, *40*, 12533.
21. Moon, O. M.; Kang, B. C.; Lee, S. B.; Boo, J. H.; *Thin Solid Films* **2004**, *464-465*, 164.
22. Chen, D.; Yang, D.; Wang, Q.; Jiang, Z.; *Ind. Eng. Chem. Res.* **2006**, *45*, 4110.
23. Jeong, J.-H.; Jung, D.-w.; Shin, E. W.; Oh, E.-S.; *J. Alloys Compd.* **2014**, *604*, 226.
24. Arun Kumar, D.; Merline Shyla, J.; Xavier, F.; *Appl. Nanosci.* **2012**, *2*, 429.
25. Tsou, H. T.; Kowbel, W.; *Surf. Coat. Technol.* **1996**, *79*, 139.
26. Ang, T. P.; Toh, C. S.; Han, Y.-F.; *J. Phys. Chem. C* **2009**, *113*, 10560.
27. de Andrade, F. V.; de Lima, G. M.; Augusti, R.; Coelho, M. G.; Ardisson, J. D.; Romero, O. B.; *Chem. Eng. J.* **2012**, *180*, 25.
28. Coelho, M. G.; de Lima, G. M.; Augusti, R.; Maria, D. A.; Ardisson, J. D.; *Appl. Catal., B* **2010**, *96*, 67.

*Submitted: November 11, 2016*

*Published online: March 6, 2017*